2013-10

# Observations of sound-speed fluctuations in the western Philippine Sea in the spring of 2009

Colosi, John A.

J. Acoust. Soc. Am. 134 (4), Pt. 2, (October 2013), p. 3185-3200
http://hdl.handle.net/10945/48421

# Observations of sound-speed fluctuations in the western Philippine Sea in the spring of 2009

John A. Colosi[a)]
*Department of Oceanography, Naval Postgraduate School, Monterey, California 93943*

Lora J. Van Uffelen
*Department of Ocean and Resources Engineering, University of Hawaii, Honolulu, Hawaii, 96822*

Bruce D. Cornuelle, Matthew A. Dzieciuch, and Peter F. Worcester
*Scripps Institution of Oceanography, University of California at San Diego, La Jolla, California, 92037*

Brian D. Dushaw
*Applied Physics Laboratory, University of Washington, Seattle, Washington, 98105*

Steven R. Ramp
*Soliton Ocean Services Inc., Carmel, California 93921*

(Received 5 October 2012; revised 2 January 2013; accepted 8 January 2013)

As an aid to understanding long-range acoustic propagation in the Philippine Sea, statistical and phenomenological descriptions of sound-speed variations were developed. Two moorings of oceanographic sensors located in the western Philippine Sea in the spring of 2009 were used to track constant potential-density surfaces (isopycnals) and constant potential-temperature surfaces (isotherms) in the depth range 120–2000 m. The vertical displacements of these surfaces are used to estimate sound-speed fluctuations from internal waves, while temperature/salinity variability along isopycnals are used to estimate sound-speed fluctuations from intrusive structure often termed spice. Frequency spectra and vertical covariance functions are used to describe the space-time scales of the displacements and spiciness. Internal-wave contributions from diurnal and semi-diurnal internal tides and the diffuse internal-wave field [related to the Garrett–Munk (GM) spectrum] are found to dominate the sound-speed variability. Spice fluctuations are weak in comparison. The internal wave and spice frequency spectra have similar form in the upper ocean but are markedly different below 170-m depth. Diffuse internal-wave mode spectra show a form similar to the GM model, while internal-tide mode spectra scale as mode number to the minus two power. Spice decorrelates rapidly with depth, with a typical correlation scale of tens of meters.
[http://dx.doi.org/10.1121/1.4818784]

PACS number(s): 43.20.Hq, 43.30.Es, 43.30.Ft [TFD] Pages: 3185–3200

## I. INTRODUCTION

In deep water acoustic propagation, acoustic variability is driven by sound-speed heterogeneities due to many oceanographic processes including internal waves (Flatté *et al.* 1979), internal tides (Dushaw *et al.*, 1995; Dushaw *et al.*, 2011), spicy thermohaline structure (Dzieciuch *et al.*, 2004), and eddies (Cornuelle *et al.*, 1985; Wolfson and Tappert, 2000). To predict the statistics of acoustic fields, it is necessary to have oceanographic models that can capture the relevant ocean scales that affect acoustic propagation. The purpose of this study is to quantify the basic scales of sound-speed variability in the Philippine Sea to aid in the development of useful ocean acoustic models. The fundamental acoustics context of this work is the question whether ocean acoustic model shortcomings are due to incorrect acoustic propagation physics or incorrect oceanographic inputs.

For deep water environments, it is well known that there is a random field of internal gravity waves whose spectrum is relatively well described by a "universal" spectrum termed the Garrett–Munk (GM) spectrum (Munk, 1981). However the GM model is a fit to many ocean observations and thus deviations from the GM model that might be expected in the Philippine Sea consist of variability in the internal-wave energy by factors of order 2, changes in the spectral slopes of order tens of percent, and differences in the internal wave modal bandwidth parameter (denoted by the parameter $j_*$). Internal tides are also known to fill the world ocean and they are particularly energetic where barotropic tidal currents cross abrupt topography (Müller and Liu, 2000). In the Philippine Sea, the Luzon Strait and Mariana Islands Arc are known to be active but variable generation sites for internal tides (Ramp *et al.*, 2010; Zhang *et al.*, 2011; Li and Farmer, 2011; Kerry *et al.*, 2012). Unlike GM-like internal waves, internal tides can be modeled more or less deterministically using regional models that carefully treat the sensitive topographic generation processes and the inherent modulation from eddies and fronts (Merrifield and Holloway, 2002). Similarly, increasingly accurate realizations of eddy activity are being obtained using high resolution ocean models that assimilate satellite altimetry and other data. Last spicy

[a)]Author to whom correspondence should be addressed. Electronic mail: jacolosi@nps.edu

thermohaline structure lies in between the deterministic and stochastic realms; spicy structure associated with eddy filaments may in fact be deterministically modeled (Todd *et al.*, 2012) while spicy structure associated with mixed layer and upper ocean processes may be more fundamentally stochastic (Ferrari and Rudnick, 2000). The Philippine Sea is expected to have strong spice features because it is a cross roads of several different water masses, there is an energetic eddy field, and there is strong surface wind forcing (Rudnick *et al.*, 2011). Ocean acousticians and oceanographers need observations of the fundamental space and time scales of these processes, such as is provided in this manuscript, to help guide model development; this development may be as easy as estimating certain parameters in the GM model or as difficult as building a data assimilating ocean model.

This study utilizes oceanographic observations from two ocean-acoustic moorings deployed in the western Philippine Sea during April and early May 2009. To better understand the oceanographic environment affecting acoustic transmissions between the moorings, they were instrumented with densely spaced temperature (T), conductivity (C), and pressure (P) instruments between 100 and 2000-m depth, as well as Acoustic Doppler Current Profilers (ADCPs) in the upper 300-m. The data obtained on these instruments are used here to examine the sound-speed variability during this month-long deployment. From these observations, we find that the Philippine Sea does indeed have a random internal-wave field that closely resembles the GM model. The overall energy of the random internal-wave field is roughly 1.4 times the standard GM level and the high frequency and high internal wave mode number spectra of these fluctuations follow nearly exactly the GM power law of frequency and mode number to the minus two power. However for the lower frequencies, near the inertial frequency and between the tide lines, the spectral energy shape is somewhat flatter than the minus two power law, and for the lowest internal wave mode numbers between 1 and 5, there are additional spectral shape anomalies with regards to the GM spectrum. The random internal waves have nearly identical statistical behavior at the two moorings, suggesting some degree of horizontal homogeneity, and measurements of currents at the two moorings reveal that the random internal waves are horizontally isotropic as well. Philippine Sea diurnal and semidiurnal internal tides are observed to have nearly equal energy compared with the random internal waves. A significant amount of energy is found at tidal harmonic frequencies, thus indicating nonlinearities. The internal tide modal content is seen to be more complex than the anticipated mode 1 dominance. In fact, the distribution of modal energies goes roughly as mode number to the minus two power, much like the high mode random internal waves. While the spectral properties of the internal tides are similar at the two moorings, there are distinct differences in diurnal and semidiurnal energy levels at the two. This spatial inhomogeneity may be due to an interference pattern generated by different internal tide bathymetric sources. With regards to eddies (or sub inertial variability), the duration of our observations was too short to reveal detailed statistical properties of the eddies. Last, on one of the moorings spicy thermohaline sound-speed fluctuations along isopycnals could be measured in the depth range 100–500 m. The Philippine Sea is known for its comingling of several different water masses, its active eddy field, and its strong wind induced surface mixing, all factors that can produce strong T and salinity (S) variations along isopycnals (spice). Contrary to this expectation, the observed spice sound speed variations over the duration of our observations were weak compared to the other processes.

The organization of this paper is as follows. Section II describes the observations and the calculations necessary to quantify sound-speed variability from isopycnal displacements and spicy thermohaline structure. Frequency spectra of the displacement and spice observations are presented in Sec. III, as well as the depth dependence of the sound-speed variance. In Sec. IV the vertical structure of displacement and spice variations is analyzed in terms of vertical covariance functions and in some cases vertical internal wave mode number spectra. Summary and conclusions are given in Sec. V.

## II. THE EXPERIMENT

Between 2009 and 2011 an interdisciplinary and multi-institutional field program was carried out in the north western Philippine Sea to study deep water, long-range acoustic propagation and ambient noise (Worcester *et al.*, 2013). This effort included a month-long 2009 pilot study/engineering test (PhilSea09), a year-long 2010–2011 Philippine Sea Experiment (PhilSea10) and an Ocean Bottom Seismometer Augmentation of the PhilSea10 experiment (OBSAPS). Of relevance to this work was the considerable effort undertaken to make detailed measurements of the time evolving ocean sound-speed field so that the observed acoustic data could be interpreted in terms of the oceanographic processes such as random internal waves, internal tides, spicy thermohaline structure, and mesoscale eddies. This paper presents results for the PhilSea09 pilot study in which a single source (T1) and a single receiver mooring (DVLA) were deployed. Future publications will address the seven mooring, full year PhilSea10 records.

### A. PhilSea09 observations

In the PhilSea09, the DVLA and T1 moorings collected acoustic and oceanographic data from 5 April through 8 May 2009. They were located at 21° 21.8978′N, 126° 01.02541′E, and 22° 57.6014′N, 126° 33.7722′E, respectively, and the water depths were 5530-m at the DVLA and 6059-m at T1. The oceanographic instrumentation on these two moorings is listed in Table I. This instrumentation, measuring T, S, and P every minute, was used to track the vertical displacement of surfaces of constant potential density (isopycnals), since the motion of these surfaces are due to internal waves and eddies. Vertical displacements, $\xi$, induce sound-speed fluctuations according to the kinematic equation $\delta c = \xi(dc/dz)_{p\xi}$, where $(dc/dz)_p$ is the potential sound speed gradient (Flatté *et al.*, 1979). Variations of temperature and salinity along the potential density surfaces, spice, also cause sound-speed fluctuations since temperature and salinity anomalies are compensating in density but reenforcing in sound speed (Dzieciuch *et al.*, 2004). Tracking

TABLE I. Oceanographic instrumentation for the (left) DVLA and (right) T1 moorings. MicroCat instruments are Seabird Electronics models SBE37-SM and SBE37-SMP (pumped), while MicroTemp instruments are model SBE39. The SBE instruments sampled the ocean at 1 min intervals. Instruments were deployed at depths derived from WKB baroclinic scaling. The two ADCPs deployed on the T1 mooring were in an up/down looking configuration, while the single ADCP on the DVLA mooring was in an up looking orientation. The ADCPs sampled the ocean at 20-min intervals.

| DVLA | | T1 | |
|---|---|---|---|
| Depth (m) | Instrument | Depth (m) | Instrument |
| 340 | ADCP (150-kHz) | 200 | 2 ADCP (300-kHz) |
| 90 | SBE37-SMP | 150 | SBE37-SM |
| 120 | SBE37-SMP | 180 | SBE39 |
| 150 | SBE37-SMP | 210 | SBE37-SM |
| 180 | SBE37-SMP | 240 | SBE39 |
| 210 | SBE37-SMP | 270 | SBE37-SM |
| 240 | SBE37-SMP | 300 | SBE39 |
| 270 | SBE37-SMP | 330 | SBE37-SM |
| 310 | SBE37-SMP | 370 | SBE39 |
| 350 | SBE37-SMP | 410 | SBE37-SM |
| 380 | SBE37-SMP | 440 | SBE39 |
| 430 | SBE37-SMP | 490 | SBE37-SM |
| 470 | SBE37-SMP | 530 | SBE39 |
| 510 | SBE37-SMP | 570 | SBE37-SM |
| 560 | SBE37-SM | 620 | SBE39 |
| 610 | SBE37-SM | 670 | SBE37-SM |
| 670 | SBE37-SM | 730 | SBE39 |
| 720 | SBE37-SM | 780 | SBE37-SM |
| 790 | SBE37-SM | 850 | SBE39 |
| 860 | SBE37-SM | 920 | SBE37-SM |
| 930 | SBE37-SM | 990 | SBE37-SM |
| 1010 | SBE39 | 1070 | SBE39 |
| 1100 | SBE39 | 1160 | SBE39 |
| 1210 | SBE39 | 1270 | SBE39 |
| 1330 | SBE39 | 1380 | SBE39 |
| 1470 | SBE39 | 1520 | SBE39 |
| 1640 | SBE39 | 1690 | SBE39 |
| 1850 | SBE37-SM | 1900 | SBE39 |
| 2150 | SBE39 | 2190 | SBE39 |
| 2630 | SBE39 | 2660 | SBE39 |
| 4990 | SBE37-SMP | 4950 | SBE39 |

isopycnals, however, requires accurate observations of salinity. To this end, the DVLA mooring contained a dense array of Seabird SBE37-SMP instruments in the upper ocean (roughly 100-m to 520-m) that, due to their pumping capability, can resolve the detailed salinity structure expected to exist in this region. To utilize the remainder of the observations (primarily temperature and pressure) on the DVLA and the T1 moorings, approximations are required. Where spiciness is weak, surfaces of constant potential temperature (isotherms) are accurate surrogates for isopycnals, and we find that over much of the water column the weak spice approximation is quite good.

In addition to the T, S, and P sensors, ADCPs on the DVLA and T1 moorings were used to quantify upper ocean internal-wave-induced currents. This information was used to cross validate internal-wave spectra derived from isopycnal displacements, and to check the assumption of horizontal isotropy for the random GM-like waves (See Sec. III A). The upward looking, 150 kHz ADCP on the DVLA provided current observations over the depth range 350–100 m with a sample interval of 20 min. The T1 mooring had two 300-kHz ADCPs deployed in upward and downward looking orientations, providing current observations over the depth range 145–270 m, again with a sample interval of 20 min.

Figure 1 shows the mean profiles of T, S, sound speed, buoyancy frequency, potential density, and potential sound speed gradient derived from the DVLA observations in the upper 2000-m, and these profiles are compared to the average of 16 nearby CTD casts obtained during the mooring deployments and recoveries. In the temperature panel of Fig. 1, the mean profile from the T1 mooring is also shown. Given the intense variability in this region, the comparison between the mooring averages and the CTDs is reasonable. A strong, broad thermocline is present between the surface and 1000 m. The mean salinity structure has a near-surface maximum close to 200 m and a minimum close to 500 m. This structure gives rise to a well stratified water column with a maximum buoyancy frequency of roughly 6 cph. Importantly for the acoustics, the salinity structure with its mid-water minimum gives rise to a maximum potential sound speed gradient close to the 500-m depth.

### B. Displacement and spice analysis

The techniques for isopycnal and spice analysis utilized in this manuscript were recently presented for a shallow water environment (Colosi *et al.*, 2012). Therefore, the description of the methodology here will be rather terse, and the interested reader should refer to Colosi *et al.* (2012) for more specific details.

In the depth range 100–500 m where the SBE37-SMP instruments were located, potential density (Talley *et al.*, 2011) referenced to the 300-decibar (db) level, $\sigma_{300}[z(t), t]$, was computed. Here $z(t)$ represents the variable depth of the instrument due to mooring motion. The 300 db reference was chosen because it is roughly half-way between the shallowest and deepest SBE37-SMP instruments. From the potential density data, the depths of 25 isopycnals, $z(t, \sigma_{300})$, between 1025 and 1027.4 kg/m$^3$ were tracked using depth-linear interpolation. (See Colosi *et al.*, 2012, for a discussion of the limitations of linear interpolation.) Potential temperature, $\theta_{300}(t, \sigma_{300})$, and salinity, $S(t, \sigma_{300})$, variations along the isopycnals (spice) were obtained by linear interpolation of the original $\theta_{300}$ and S data onto the computed isopycnal depth $z(t, \sigma_{300})$. Potential temperature is used here to account for the adiabatic temperature changes as the water parcels are displaced vertically, which is also the rationale for using potential density to track the vertical displacements of the isopycnals.

To estimate the error in the isopycnal tracking the $\theta_{300}(t, \sigma_{300})$ and $S(t, \sigma_{300})$ values were used to recompute potential density. The rms differences between the recomputed densities and the target densities are shown in Table II, column five; the small differences show that the linear isopycnal tracking is a good approximation. This tracking error can also be expressed as a depth error by dividing the root-mean-square (rms) density difference by the mean

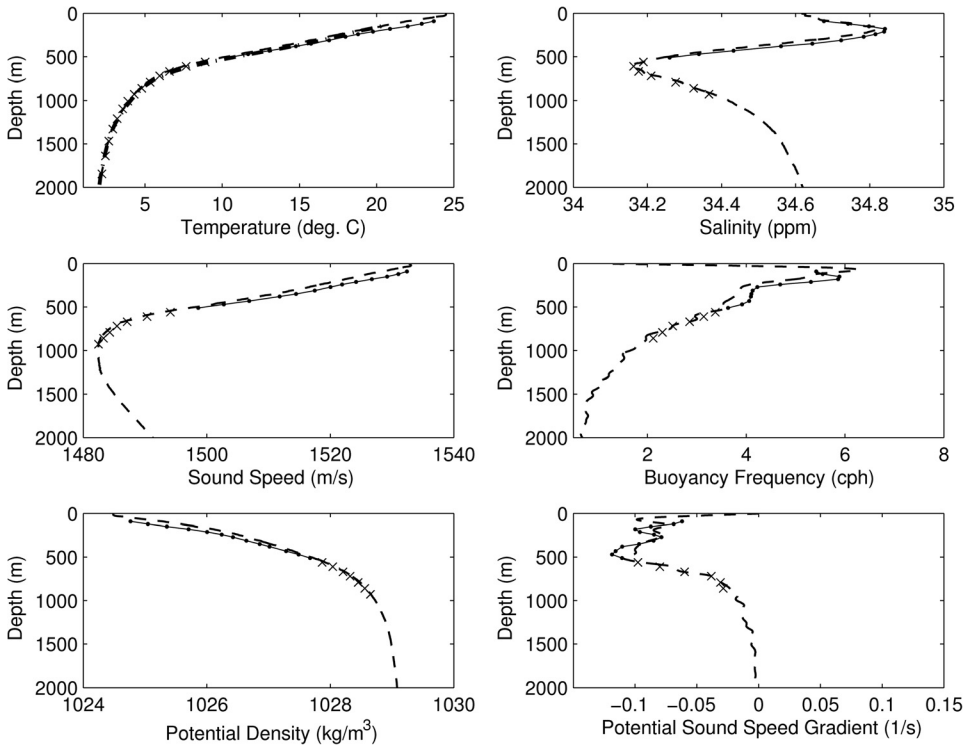


FIG. 1. Mean profiles of temperature, salinity, sound speed, buoyancy frequency, potential density, and potential sound-speed gradient. Values derived from the DVLA SBE37-SMPs are shown with dots, while DVLA values derived from either SBE37-SMs or SBE39s are shown with crosses. Average profiles derived from 16 CTD casts made in the timeframe of the deployment and recovery of the moorings are shown with dashed lines. The average temperature profile from T1 is plotted with a dash-dot in the upper left panel, but the curve lies almost directly on the CTD curve.

density gradient (Table II, column six). The depth error is seen to be quite small, with a maximum value of 0.6 m.

Figure 2 shows the month-long DVLA mooring depth-time-series of potential density, $\sigma_{300}[z(t), t]$, and salinity $S[z(t), t]$ with a few tracked isopycnals superimposed. The density field shows the typical random variations associated with Garrett–Munk (GM) type random internal waves, but more noticeable are the strong fluctuations at tidal frequencies, particularly the diurnals with periods close to 1 day. In addition, a surface-intensified sub-inertial or mesoscale variation is seen. For the salinity field, variations similar to the density field are evident. However, in the upper ocean between days 105 and 120 a significant feature with enhanced salinity passed by the DVLA. The associated gradients of salinity along the isopycnals indicate spicy variability. Table II provides mean and rms values of spicy $\theta_{300}(t, \sigma_{300})$ and $S(t, \sigma_{300})$ as well as spicy sound-speed variation on the isopycnals (Also see Sec. III). These values indicate rather small spice variations except for the shallowest isopycnals. Larger spice variations are expected in the upper ocean where strong spice anomalies are generated by precipitation, evaporation, and wind-forced mixing. The values observed here, however, are much smaller than those observed by Ferrari and Rudnick (2000) in the winter eastern North Pacific Ocean and by Colosi *et al.* (2012) on the summer New Jersey continental shelf of the United States. The small values of spice come as some surprise since the Philippine Sea is known to be a cross roads of several

TABLE II. Observed isopycnal statistics for every other tracked isopycnal. The first column gives the chosen isopycnal density, and the second, third and fourth columns are the mean isopycnal depth, potential temperature, and salinity. The fifth column is the rms uncertainty in isopycnal tracking (See text for details), and the sixth column gives the depth error associated with the tracking uncertainty. The seventh, eighth, and ninth columns give the spicy rms temperature, salinity, and sound speed fluctuations along the isopycnal. The rms values given in columns seven through nine only include contributions from frequencies between $f$ and $N$.

| $\sigma_{300}$ (kg/m$^3$) | $\langle z \rangle$ (m) | $\langle \theta_{300} \rangle$ (°C) | $\langle S \rangle$ (psu) | $\delta\sigma_{300}$ (kg/m$^3$) | $\delta\sigma_{300}/(d\bar{\sigma}_{300}/dz)$ (m) | $\delta\theta_{rms}$ (°C) | $\delta S_{rms}$ (psu) | $\delta c_{rms}$ (m/s) |
|---|---|---|---|---|---|---|---|---|
| 1025.0 | 127.8 | 23.15 | 34.76 | 0.001 | 0.10 | 0.10 | 0.04 | 0.30 |
| 1025.2 | 146.6 | 22.53 | 34.78 | 0.001 | 0.03 | 0.07 | 0.03 | 0.21 |
| 1025.4 | 156.6 | 21.91 | 34.81 | 0.001 | 0.10 | 0.05 | 0.02 | 0.14 |
| 1025.6 | 171.9 | 21.26 | 34.84 | 0.001 | 0.12 | 0.04 | 0.01 | 0.12 |
| 1025.8 | 188.7 | 20.56 | 34.85 | 0.001 | 0.14 | 0.03 | 0.01 | 0.09 |
| 1026.0 | 208.6 | 19.80 | 34.84 | 0.001 | 0.13 | 0.02 | 0.01 | 0.07 |
| 1026.2 | 233.5 | 18.98 | 34.82 | 0.001 | 0.12 | 0.02 | 0.01 | 0.05 |
| 1026.4 | 265.4 | 18.10 | 34.79 | 0.001 | 0.15 | 0.02 | 0.01 | 0.05 |
| 1026.6 | 302.5 | 17.12 | 34.74 | 0.001 | 0.20 | 0.02 | 0.01 | 0.07 |
| 1026.8 | 340.5 | 16.06 | 34.67 | 0.001 | 0.23 | 0.03 | 0.01 | 0.09 |
| 1027.0 | 378.2 | 14.84 | 34.57 | 0.002 | 0.34 | 0.03 | 0.01 | 0.10 |
| 1027.2 | 415.0 | 13.57 | 34.47 | 0.002 | 0.56 | 0.03 | 0.01 | 0.11 |
| 1027.4 | 453.5 | 12.24 | 34.38 | 0.002 | 0.51 | 0.04 | 0.01 | 0.12 |

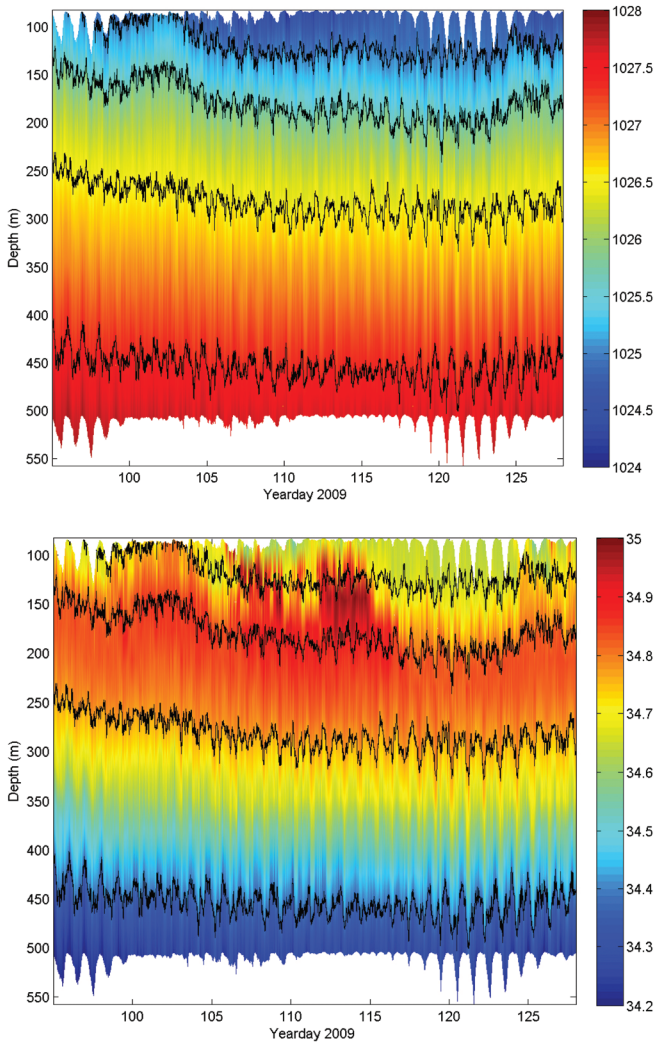


FIG. 2. Depth/time series of (top) observed potential density ($\sigma_{300}$) and (bottom) salinity at the DVLA. Superimposed on the plots are the isopycnal depths for densities of 1025, 1025.7, 1026.5, and 1027.4 kg/m$^3$.

different water masses (Kaneko *et al.*, 2001), evaporation and precipitation are large, and wind forcing is generally strong. In a $\theta$-$S$ diagram utilizing the PhilSea09 CTD data (Fig. 3), regions of large spice are evident where there is a large spread of points across a contour of constant potential density for example the region $\theta_{300} > 18\,^{\circ}$C, and somewhat less so $4^{\circ} < \theta_{300} < 10\,^{\circ}$C. Correspondingly, regions of weak spice are where the spread in the $\theta$-$S$ curve is small, for example, in the regions $10^{\circ} < \theta_{300} < 18\,^{\circ}$C and $0^{\circ} < \theta_{300} < 4\,^{\circ}$C. Using information from Table II, Fig. 3, and the CTD profiles, specific spice-rich depth regions can be identified. Here the data suggest that stronger spice regions are confined to the depths above 200-m, and between 500- and 800-m.

The weakness of spice in the depth ranges 200–500 m and 800–6000 m suggests that isopycnals at the DVLA and T1 can be accurately tracked in these depth ranges using temperature alone. In the depth region 500–800 m there is the possibility of spice contamination in displacements estimated from temperature alone, but we ignore this issue to compute isotherm depths at the DVLA and T1 moorings between the depth region 200–2000 m. Isotherms cannot be easily tracked below 2000 m because of the weak temperature gradients in the deep ocean. The calculation proceeds along the same lines as the one for isopycnals, that is potential temperature referenced to 300 db, $\theta_{300}[z(t), t]$, is computed on the moorings and then isotherm depths, $z(t, \theta_{300})$ at selected values of potential temperature are computed from this data using depth-linear interpolation. The calculation of potential temperature requires salinity, and where no *in situ* values were available, the data from the mean of the CTD casts were used (See Fig. 1, upper right panel). Comparisons of the fluctuating isopycnal and isotherm depths on the DVLA between 200- and 450-m depth (not shown) support the assumption that the isotherms are an excellent surrogate for isopycnals.

Figure 4 shows depth-time-series of isopycnal displacements estimated for the depth range of 100–1000 m using

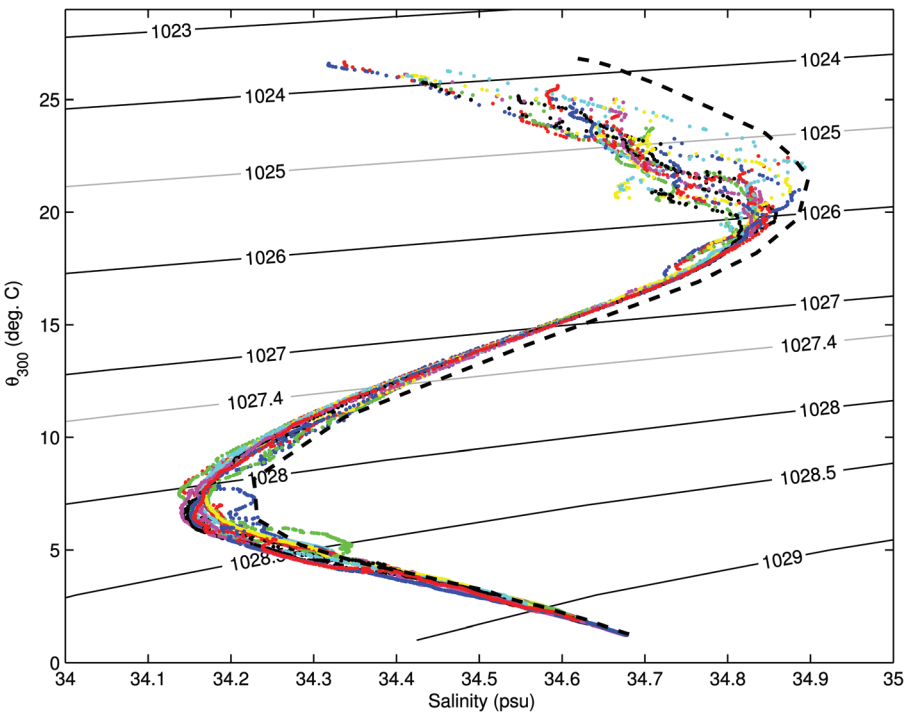


FIG. 3. Potential temperature, $\theta_{300}$, is plotted against salinity (S) for 16 CTD profiles obtained during the PhilSea09 (color dots). Results for the Annual World Ocean Atlas are shown for comparison (dash), and contours of potential density, $\sigma_{300}$, between 1023 and 1029 kg/m$^3$ are shown for reference. The gray contours at 1025 and 1027.4 kg/m$^3$ correspond to the shallowest and deepest isopycnals tracked in this analysis, and points near these contours have average depths of 130 and 450-m, respectively (See Table II). Points near the 1024 kg/m$^3$ contour are close to the ocean surface, while points close to 1028.5 are near 800-m depth.

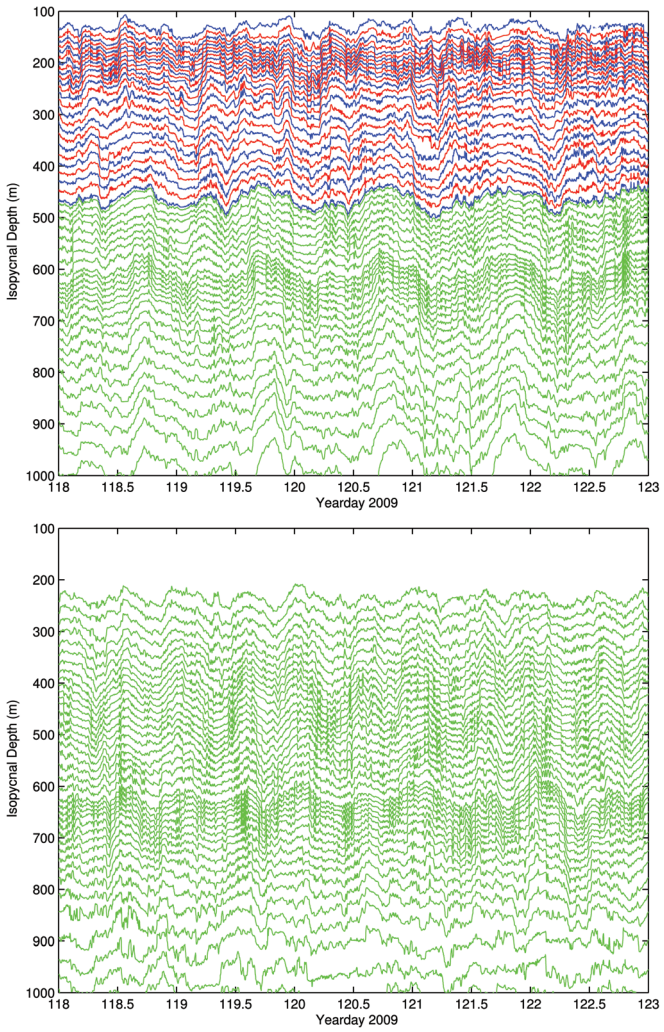


FIG. 4. A 5 day section showing tracked isopycnals (blue and red), and tracked isotherms (green) in the upper 1000-m, for the (top) DVLA and (bottom) the T1 mooring.

both $T$ and $S$ (red and blue lines), and $T$ only (green lines). The upper panel displays results from the DVLA, while the lower panel gives T1 results. While Fig. 4 only shows variations down to 1000-m, isotherms for both the DVLA and T1 were tracked down to roughly 2000 m depth. Extending the displacement measurements down to 2000 m provides much needed information to resolve the modal content of the fluctuations (Sec. IV). In Fig. 4 displacements are shown only over 5-days so that details of the fluctuations are more evident. The DVLA displacement estimates transition smoothly between the regions where isopycnal data ends and isotherm data begins. In addition, Fig. 4 shows that there are periods and specific depth regions in which the displacements change quite rapidly in time. It will be shown later that this rapid change is associated with nonlinear steepening of the internal tide, which generates tidal frequency harmonics (See Sec. III).

Figure 5 shows details of the spicy sound-speed and $T$, $S$ fluctuations along one of the shallowest and most spicy isopycnals in the DVLA analysis. All three curves shown in Fig. 5 are nearly perfectly correlated because these are values along an isopycnal where $T$ and $S$ anomalies are exactly compensating; the three plots are shown here to emphasize the order of magnitude of the effects and to underscore the temporal variability. Importantly, because the isopycnals are moving vertically, the spicy sound-speed fluctuations shown in Fig. 5 are computed using the mean depth of the isopycnal, $\bar{z}(\sigma_{300})$. The time evolution of the spice is quite intermittent in nature with periods of strong and weak variability. The intermittency and pattern of spice variability (Fig. 5) is remarkably similar to that observed in shallow water on the New Jersey continental shelf (Colosi *et al.*, 2012, Fig. 4).

## III. FREQUENCY SPECTRA AND ANALYSIS OF VARIANCE

In this section the time scales of isopycnal displacement and spice variability are addressed using frequency spectra.

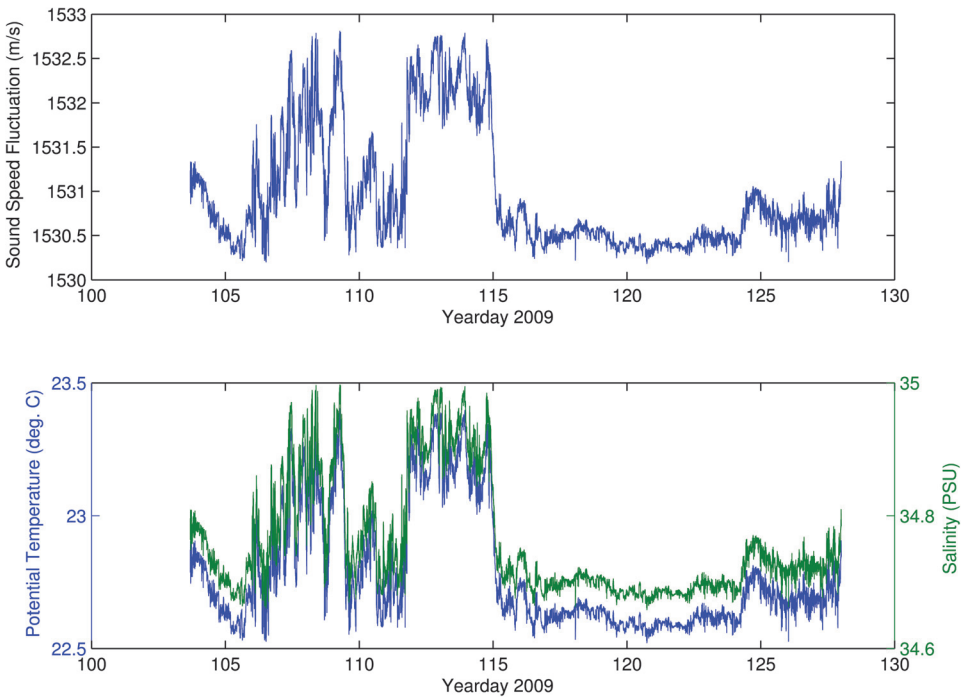


FIG. 5. Temporal fluctuations along the isopycnal 1025.1 kg/m$^3$. (top) Sound-speed variability; (bottom) the highly correlated potential temperature and salinity changes.

Because there is depth inhomogeneity of these processes, we also present results that quantify the changes in strength and spectral shape as a function of depth. We start with an analysis of the displacement fields, which are primarily affected by internal waves and internal tides.

### A. Internal waves and internal tides

The observed displacement time series, $z(t, \sigma_{300})$ and $z(t, \theta_{300})$ were used to compute frequency spectra that include effects from eddies, random internal waves, and internal tides. Before the spectral analysis was performed the isopycnal displacement time series were low-pass filtered with a 4-pole Butterworth digital filter to eliminate signals with frequencies greater than 500 cpd (or roughly 20 cph). To minimize side band leakage from the energetic low frequencies, spectrograms for the filtered isopycnals were computed using the multi-taper method of Thompson (Percival and Walden, 1993; Thompson, 1982) with an estimated time-bandwidth product of 4 and a record length of 24 $M_2$ tidal cycles or roughly 12.42 days. The spectrograms were averaged over the 33-days observation period using half-overlapping segments to provide a power spectral density (PSD) estimate, $S_{\xi}(\omega, \bar{z})$, for each of the 25 isopycnal densities where $\bar{z}$ is the mean depth of the isopycnal or isotherm as appropriate. The left-hand panel of Fig. 6 shows the DVLA displacement spectra averaged over two depth intervals, 130–285 m and 300–455 m. The displacement spectra have a spectral gap between the frequencies associated with eddies (sub-inertial variability) and those associated with internal waves (super-inertial variability). Also prominent in the spectra are strong discrete diurnal and semidiurnal tide lines as well as tidal harmonics; the harmonics are associated with nonlinearities in the internal tides, evident from regions in Fig. 4 where tidal steepening is present. In the so-called continuum range between frequencies of roughly 4 to 40 cpd, a power law shape is seen with a spectral slope of $-2.0 \pm 0.1$, which is consistent with the GM value of $-2.0$. In the frequency range between 4 cpd and the Coriolis frequency $f$ (0.7488 cpd), the continuum between the tide lines is somewhat diminished from what would be expected by extension of the $-2$ power law. This effect has been noted by Levine (2002), and a latitude-dependent correction to the GM model in this low frequency region has been put forward.[1] For frequencies greater than 100 cpd the spectra cut

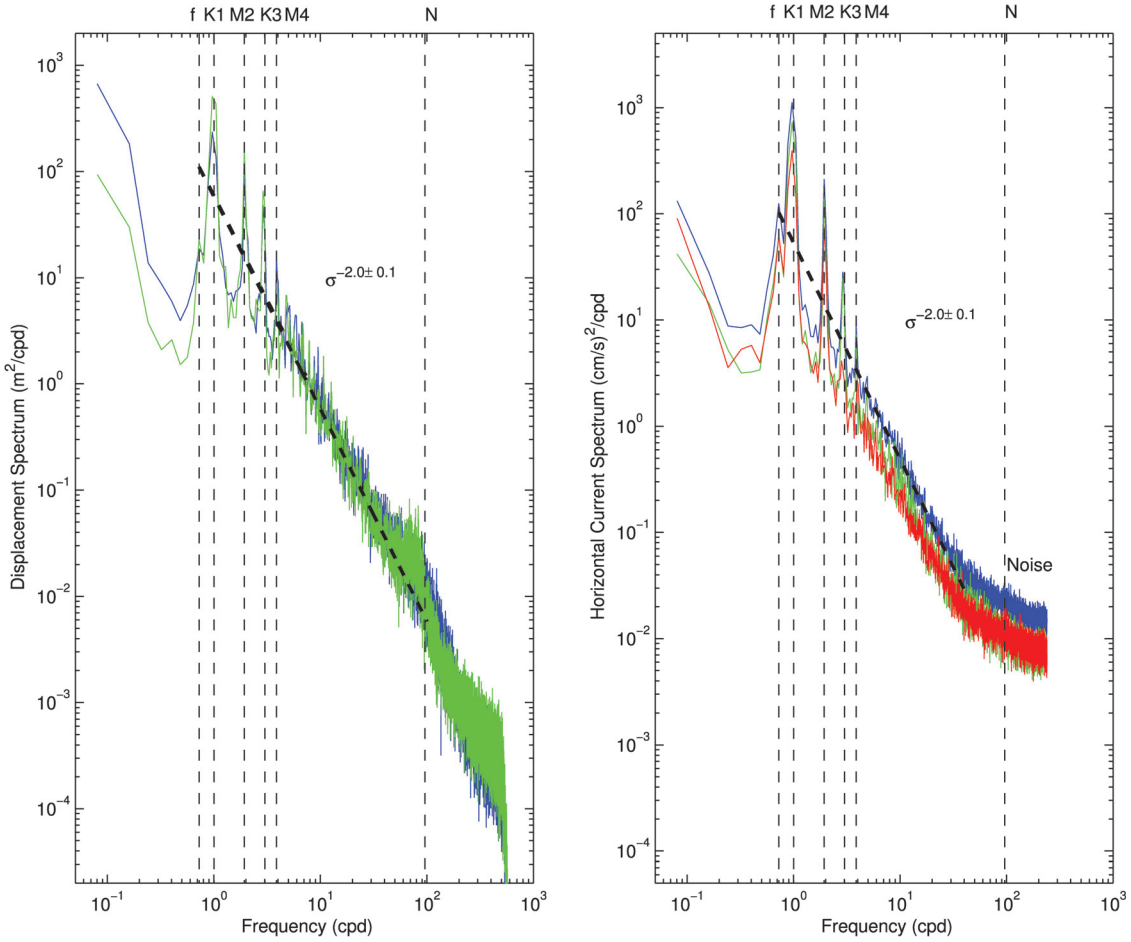


FIG. 6. Spectra of (left) DVLA displacement and (right) horizontal current. The displacement spectra are averaged over the depth regions 130–285 m (blue) and 300–455 m (green). Power law fits to the spectra in the frequency range 3.0 to 30 cpd are shown (dash). The horizontal current spectra shown are for the east–west component (green), north–south component (red), and the sum of these two (blue). The current spectra are an average over observations taken in the depth range 170–320 m. A power law fit to the blue curve is shown (dash). Important frequencies are shown at the top of the graphs with associated vertical dash lines: $f$ the Coriolis frequency, $N$ a typical buoyancy frequency, K1 a diurnal tide frequency, M2 a semidiurnal tide frequency, K3 the third harmonic of K1, and M4 a second harmonic of M2.

off rapidly, since these frequencies are at or above the buoyancy frequency cut off. The spectra averaged over the two different depth ranges are quite similar, except for a small shift in energy level, and expected differences near the buoyancy frequency cut off, which changes with depth [see Fig. 1, $N(z)$ profile].

As a further check on the quality of the $T$ and $S$ derived displacement observations, spectra for horizontal current were computed from the DVLA ADCP observations. The right-hand panel of Fig. 6 shows these spectra averaged over the depth interval 175–318 m. The displacement and horizontal current spectra should be identical except near the inertial frequency (Munk, 1981). Here the spectra compare extremely well, except at higher frequencies where the ADCP spectra are corrupted by noise. The two spectra have the same tidal constituents and roughly the same power law behavior in the continuum region. The horizontal current spectra show that the fluctuations of the non-tidal internal waves are roughly isotropic due to the strong similarity of the north/south and east/west current spectra. Displacement and horizontal current spectra computed from the T1 mooring (not shown) are qualitatively similar to the results from DVLA, but with a larger discrepancy between the displacement and horizontal current power law exponents, which are $-1.9 \pm 0.1$ and $-1.7 \pm 0.1$, respectively.

The strength of random internal wave and internal tide displacement fluctuations depend strongly on depth. To quantify this depth-dependent variability, which is critical for ocean acoustic applications, we present here the rms displacement and associated sound speed fluctuation estimates. Estimates of vertical covariances and spectra will be given in Sec. IV. Using the displacement time series going down to 2000-m depth, Fig. 7 shows the rms displacement statistics from the DVLA and T1 moorings due to Garrett-Munk-like random internal waves and internal tides. The internal tides were estimated using a tidal fit of four diurnal (O1, K1, P1, and Q1) and four semidiurnal (M2, S2, N2, and K2) constituents. The strength of the random internal waves was computed by de-tiding the displacement time series using the aforementioned tide fits, calculating a spectrum of the detided records and then integrating the spectrum from $f$ to $N$. With regards to the random internal wave component, the results from the DVLA and T1 are nearly identical and are consistent with the baroclinic Wentzel–Kramers–Brillouin (WKB) depth scaling relation $\langle \xi^2 \rangle^{1/2} = \xi_0 \sqrt{N_0/N(z)}$ (Munk, 1981), where $\xi_0 = 8.6$ m, $N_0 = 3$ cph, and $N(z)$ comes from the CTD casts of Fig. 1. The random internal wave component fits the WKB model extremely well due to the rich modal content of these variations (See Sec. IV). It should also be noted that the standard GM value for $\xi_0$ is 7.3-m, so the observed internal waves have energies roughly 1.4 times the standard GM level.

With regards to the internal tides the DVLA shows the diurnal tide to be more energetic than the semi-diurnal tide while the T1 shows the opposite (Fig. 7). This result is not unexpected as the spatial pattern of the internal tide is affected by the complex geometry of the tidal generation zone(s), which can lead to an interference pattern. It should also be noted that the depth dependence of the rms internal tide displacement does not have the structure of mode 1 (Fig. 10), and thus the modal spectrum of the internal tide may be substantially more complicated than the expected mode 1 form (more on this in Sec. IV).

Last it should be noted that rms displacements must vanish at the ocean boundaries because of the internal wave boundary conditions (Munk, 1981). Therefore the increase in rms displacement with depth shown in Fig. 7 must eventually

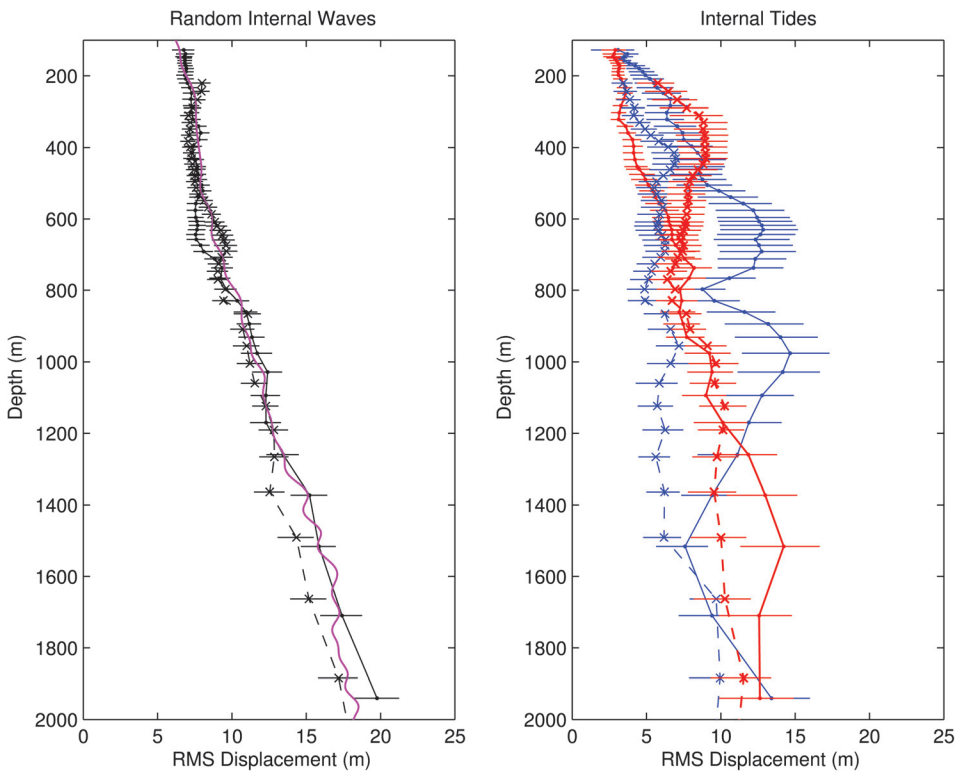


FIG. 7. Root mean square (RMS) displacement statistics for (left) random internal waves, and (right) internal tides. For the internal tides, diurnal fluctuations are plotted in blue while semi-diurnal fluctuations are shown in red. Results for the DVLA are plotted using dots and solid lines, while the T1 results are displayed using crosses and dash lines. Also shown in the left panel is the WKB estimate (magenta) utilizing a reference internal wave displacement $\xi_0$ of 8.6 m.

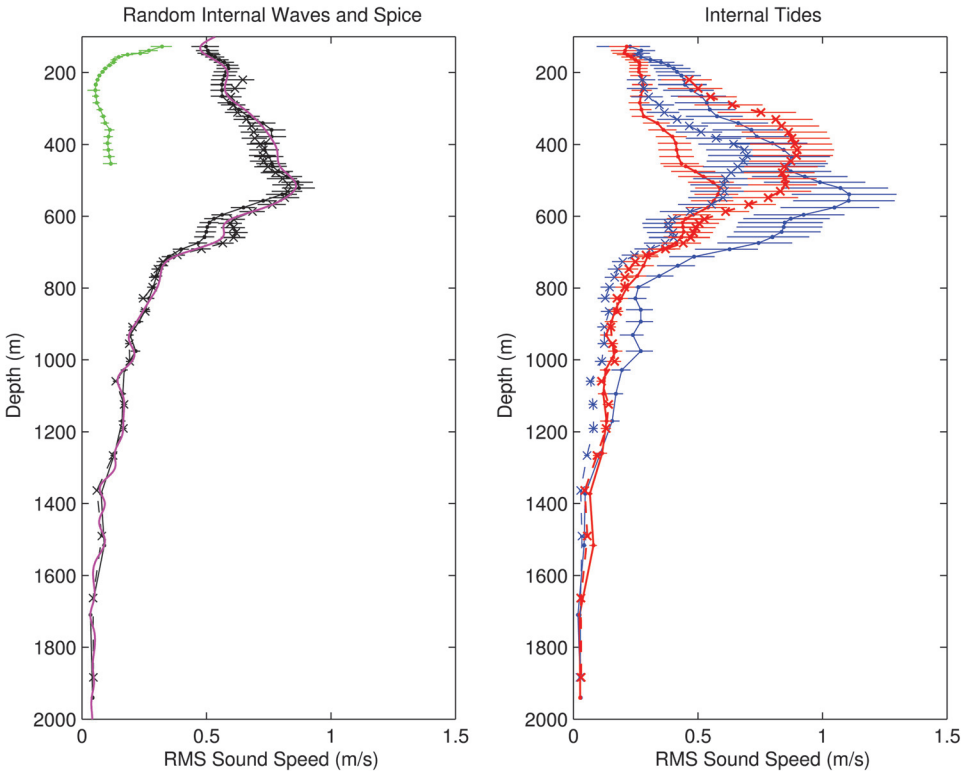


FIG. 8. Root mean square sound speed fluctuations from (left) random internal waves and (right) internal tides. The internal wave and internal tide sound-speed statistics are obtained by multiplying the rms displacements in Fig. 7 by the mean potential sound speed gradient (see Fig. 2). The identification of curves in this figure is the same as in Fig. 7. Spicy sound speed fluctuations with contributions from the frequency band between $f$ and $N$ (i.e., the internal wave band) are plotted in green in the left panel.

be reversed at large depths, and the value must diminish to zero at the ocean surface.

It is important to make some notes on the relative strengths of the fluctuations from these processes. The internal tides are of comparable magnitude to the random internal waves and thus these tides may have a strong acoustic signature. The present internal tide variability is significantly larger than that observed in the central North Pacific, where inverse acoustic methods were used to map the internal tide (Dushaw *et al.*, 1995).

Using the standard kinematic relationship connecting sound-speed perturbation to vertical displacements [$\delta c = \xi(dc/dz)_p$], the rms displacements in Fig. 7 can be displayed as an rms sound-speed fluctuation (Fig. 8). With regards to the random internal-wave-induced sound-speed fluctuation, the maximum 1 m/s rms value is comparable to observations from the central North Pacific Ocean (Beron-Vera *et al.*, 2003); however, due to the shape of the potential sound-speed gradient (Fig. 1), this maximum is near 550-m depth, while the North Pacific maximum is near 150-m depth. The internal tide fluctuations also have a peak near 500-m due to the potential sound-speed gradient.

## B. Spice

The 25 isopycnals tracked using the SBE37-SMP instruments yielded information concerning temperature and salinity variations along isopycnals (spice). The spicy $\theta_{300}(t, \sigma_{300})$ and $S(t, \sigma_{300})$ variations along the 25 tracked isopycnals are used to compute sound-speed variations along the isopycnals. As previously mentioned, because the isopycnals are moving vertically, the spicy sound-speed fluctuations are computed using the mean depth of the isopycnal, $\bar{z}\ (\sigma_{300})$, and thus the spicy sound speed is denoted by $c_S(t, \bar{z}, \sigma_{300})$. Frequency spectra of $c_S$ were computed for each isopycnal as discussed in Sec. III A, and these spectra were averaged over the depth intervals 130–165 (i.e., a depth region of relatively stronger spice) and 170–454 m (i.e., a depth region of relatively weak spice) (Fig. 9). The spice spectra in these two depth regions are quite different. The spectrum in the shallow region, where spice is relatively strong, has a slope of $-1.7 \pm 0.1$ compared to the internal-wave slope of $-2.0 \pm 0.1$, but the tidal peaks are absent. The similarity of

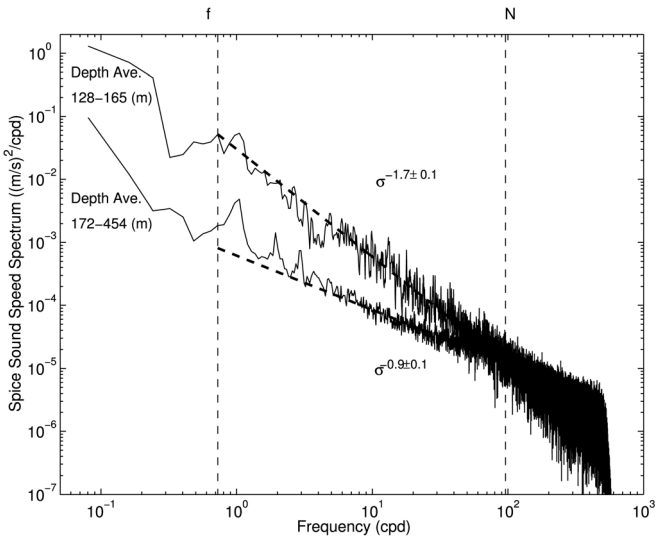


FIG. 9. Frequency spectra of sound-speed fluctuations along isopycnals (spice) averaged over depth regions 128–165 m and 172–454 m. Power law fits to the spectra in the frequency range 3.0 to 30 cpd are shown (dash). Important frequencies are shown at the top with associated vertical dash lines: $f$ the Coriolis frequency and $N$ a typical buoyancy frequency.

the power law to the internal-wave spectrum and the smearing of the tide lines is consistent with the prevailing view that the time evolution of the spice is due to the advection of these dynamically passive structures by internal-wave currents (Philipps, 1971; Garrett and Munk, 1971; Munk, 1981). Interestingly this deep water spice spectrum is quite similar in form to the spice spectrum observed in shallow water on the New Jersey shelf (Colosi *et al.*, 2012), where the slopes are essentially the same. These spectra are consistent with the view that spicy ocean features are essentially front-like (Ferrari and Rudnick, 2000), and thus, a spectral slope close to $-2$ is expected (i.e., the spectral slope of a step function). The spice spectrum in the deeper layers reveals a much flatter spectrum with a slope of $-0.9 \pm 0.1$. These spicy fluctuations are more noise-like (flat spectrum) than front-like (slope of $-2$). Because the spice is so weak in these layers the measurements of spice here may in fact be at the threshold of our measurement capability.

The spice contribution to sound-speed variance is displayed in Fig. 8 for the internal wave band. The spice contribution is quite small compared to the other processes, except perhaps in the shallowest depths observed, that is roughly 125-m to 175-m depth. The spice contribution is expected to be largest in and near the mixed layer, but we do not have measurements in that region (Fig. 3). Thus it must be concluded that the spice at the DVLA mooring is quite weak for the period of this experiment and that the sound-speed perturbations are dominated by internal tides, and random internal waves. This result is in stark contrast to the shallow water results for the New Jersey Continental shelf (Colosi *et al.*, 2012), where spice dominated the sound-speed variability with rms fluctuations from 1 to 2.5 m/s.

## IV. VERTICAL STRUCTURE

In this section the vertical spatial structure of the oceanic variability observed during the PhilSea09 experiment will be characterized. To do this, estimates of vertical covariance functions for the various oceanographic processes considered will be presented. The covariance function is an important quantity because it is an input to many acoustic fluctuation calculations. In some instances the covariance functions can be interpreted in terms of dynamical ocean modes, and in others, like spice, the analysis begins and ends with the covariance.[2] With regards to dynamical modes, following Colosi *et al.* (2012), a band-passed displacement depth/times series is written

$$\xi(z,t) = \sum_{j=1}^{J} a_j(t)\,\phi_j(z), \tag{1}$$

where $\phi_j(z)$ are the orthonormal dynamical modes associated with the particular pass-band of the displacements (i.e., diurnal or semidiurnal internal tides, random internal waves, etc.) and $J$ is the maximum mode number. Here the objective is to obtain an estimate of the energy in each mode, that is $\langle |a_j|^2 \rangle$. Thus dynamical modes can be fit to the depth time series and the mode energy can be estimated (Wunsch, 1997). For the case in which the mode amplitudes, $a_j$, are uncorrelated, the covariance function can be written

$$C(z_1,z_2) = \langle \xi(z_1)\xi(z_2) \rangle = \sum_{j=1}^{J} H(j)\phi_j(z_1)\phi_j(z_2), \tag{2}$$

where $H(j) = \langle |a_j|^2 \rangle$ is the mode spectrum. Inverting Eq. (2) directly for the mode spectrum avoids the bias that can be present in the statistics of the inversion of Eq. (1) in which the mode amplitudes are squared and averaged over time. For random internal-wave fluctuations Eq. (2) is most useful and provides a means for estimating the internal-wave mode spectrum (Colosi *et al.*, 2012), which can be compared to the Garrett–Munk model $H_{GM}(j) = N_j/(j^2 + j_*^2)$, where $N_j$ is a normalization and $j_* = 3$ (Munk, 1981). For the PhilSea09 internal tides, however, the modes are seen to be strongly correlated, and thus Eq. (1) is most useful in which the modes are directly fit to the depth time series to estimate the mode energy.

### A. Diffuse internal waves

The diffuse internal-wave field is composed of many uncorrelated internal-wave modes and frequencies (Munk, 1981). The mode shapes in general have a frequency dependence, caused primarily by the frequency dependence of mode lower turning depth, that is when $N(z) = \sigma$, where $\sigma$ is the internal-wave frequency. Because of this frequency dependence, Eq. (1) is used to represent a band-passed depth-time series in which the mode shapes change little over the selected band. The internal wave modes for a resting, linear, flat bottom ocean are given by

$$\frac{d^2\phi_j}{dz^2} + k_j^2\left[\frac{N^2(z)-\sigma^2}{\sigma^2 - f^2}\right]\phi_j = 0, \tag{3}$$

where $k_j$ is the mode horizontal wave number, $f$ is the Coriolis frequency, and the boundary conditions are $\phi_j(0) = \phi_j(D) = 0$ with $D$ being the water depth. The internal-wave modes obey the orthonormality condition $\int_0^D [N^2(z) - \sigma^2]\phi_j\phi_n dz = \delta_{jn}$. Figure 10 shows the frequency variation of internal-wave mode shapes computed using the mean CTD buoyancy frequency profile (Fig. 1), but utilizing the full water depth profile. For $f \le \sigma \le 0.2$ cph ($f = 0.0312$ cph, or a period of 32.03 h), the mode shapes are weakly dependent on frequency, especially in the depth range from the surface to 2000 m where the observations are made. For frequencies greater than 0.2 cph, the modes depend strongly on frequency because of the small values of $N$ in the deep ocean. Thus to estimate the internal-wave mode spectrum using Eq. (2), three pass-bands are chosen over which the mode shapes are roughly independent of frequency: $f \le \sigma \le 0.1$ cph, $0.4 \le \sigma \le 0.6$ cph, and $0.9 \le \sigma \le 1.1$ cph. Comparisons between these bands is important because in the GM model the mode spectrum is expected to be independent of frequency. The pass-bands are computed from the data using a 2 pole Butterworth digital filter with the roll-off frequencies given above.

Equation (2) can be cast as a matrix equation of the form

$$\mathbf{y} = \mathbf{E}\mathbf{x} + \mathbf{n}_\mathbf{y}, \tag{4}$$

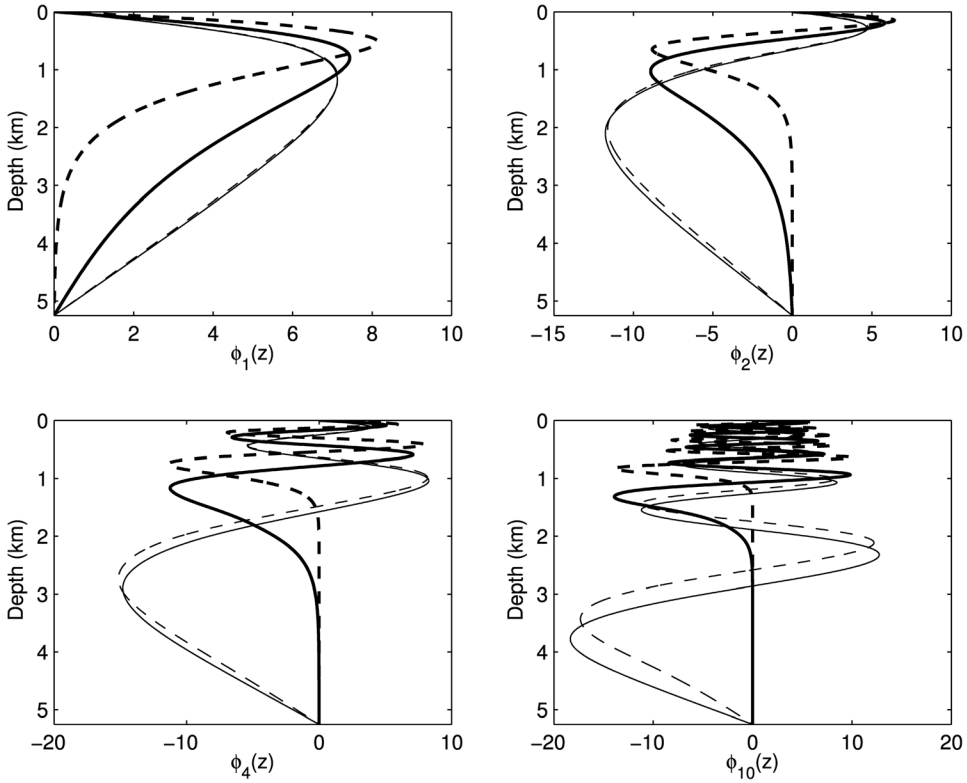


FIG. 10. Frequency dependence of PhilSea09 internal wave modes 1, 2, 4, and 10. The thin curves show frequencies of $1.05f$ (solid) and 0.2 cph (dash), while the thicker curves show $\sigma = 1$ cph (solid) and $\sigma = 2$ cph (dash).

where $\mathbf{y} = \langle \xi(z_1)\xi(z_2) \rangle$ is a vector of observed covariances, $\mathbf{E} = \phi_j(z_1)\phi_j(z_2)$ is a matrix of mode shape products, $\mathbf{x} = H(j)$ is the mode spectrum, and $\mathbf{n_y}$ is a vector of covariance uncertainties. Equation (4) is amenable to inverse methods analysis to extract estimates of the mode spectrum (and uncertainties) from estimates of the covariance function (Colosi *et al.*, 2012), but some care must be taken since $\mathbf{x}$ is non-negative. The approach here is to take the GM spectrum as an initial guess $\mathbf{x_0} = H_{GM}(j)$, and use the Gauss–Markov method to estimate corrections to the GM model. The problem is then of the form, $\delta\mathbf{y} = \mathbf{E}\delta\mathbf{x} + \mathbf{n}_y$ where $\delta\mathbf{x} = \mathbf{x} - \mathbf{x}_0$ and $\delta\mathbf{y} = \mathbf{y} - \mathbf{E}\mathbf{x}_0$. The Gauss–Markov solution for $\delta\mathbf{x}$ and its covariance $\mathbf{P}$ is thus (Munk *et al.*, 1995)

$$\delta\mathbf{x} = (\mathbf{S}^{-1} + \mathbf{E}^T\mathbf{R}^{-1}\mathbf{E})^{-1}\mathbf{E}^T\mathbf{R}^{-1}\delta\mathbf{y}, \tag{5}$$

$$\mathbf{P} = (\mathbf{S}^{-1} + \mathbf{E}^T\mathbf{R}^{-1}\mathbf{E})^{-1}, \tag{6}$$

where the *a priori* covariances for $\delta\mathbf{x}$ and $\mathbf{n}_y$ are represented by the matrices $\mathbf{S}$ and $\mathbf{R}$ respectively. For $\mathbf{S}$, a diagonal matrix is assumed that is of the form $H_{GM}(j)H_{GM}(1)$, which has a flatter drop off with mode number than the initial guess. This is done to make the uncertainty a larger fraction of amplitude for the higher modes though the scaling factor $H_{GM}(1)$ is somewhat arbitrary. The matrix $\mathbf{R}$ is also assumed diagonal, and these values are estimated from the data by computing the sampling uncertainty in the covariance estimates. This goes as the variance of the covariance estimate divided by the number of independent samples. This procedure was tested using artificially generated "data" with known spectral properties; in all cases the methodology was able to produce an estimated spectrum that was within error bars of the known spectrum.

Figure 11 shows some examples of the DVLA displacement covariance functions with error bars (i.e., the square root of the diagonal elements of $\mathbf{R}$). The covariance functions from the T1 mooring (not shown) are similar to the DVLA results. The covariances $C(z_1, z_2)$ are shown as a function of $z_2$ for two reference depths $z_1$, and for the case $z_1 = z_2$ (i.e., the variances as a function of depth). Examples for the low frequency and high frequency pass-bands are presented, since the mid-frequency results (not shown) are similar to the high frequency results. Figure 11 also shows the covariance from the initial guess (red) and the fit covariance (green). All covariances show a decay near $z_1$ with a characteristic scale of a few hundred meters, and the fit spectrum is clearly an improvement over the GM model. Note also that the vertical structure of the variance (bottom panels in Fig. 11) is different in the different pass-bands. At low frequency the variance generally increases with depth, whereas there is a peak around 1300-m at high frequency. The high frequency peak is due to the fact that for $\sigma = 1$ cph, the internal wave modes have a turning point near 1300-m depth.

The estimated mode spectra and uncertainties at the DVLA and T1, as well as the GM spectrum for the three pass-bands are shown in Fig. 12. The DVLA and T1 results are seen to be similar, suggesting that the diffuse internal-wave field is rather homogeneous over the propagation path. For mode numbers greater than 5, the estimated spectra and the GM model show roughly the same behavior, that is a decay that goes as one over the mode number squared. However for the lowest modes, modes 1 through 5, there are dramatic differences between the GM model and the observations. In particular mode 1 has much less energy than is predicted by GM, and there is a peak in the spectrum near mode 3. With regards to these lower modes there is also a

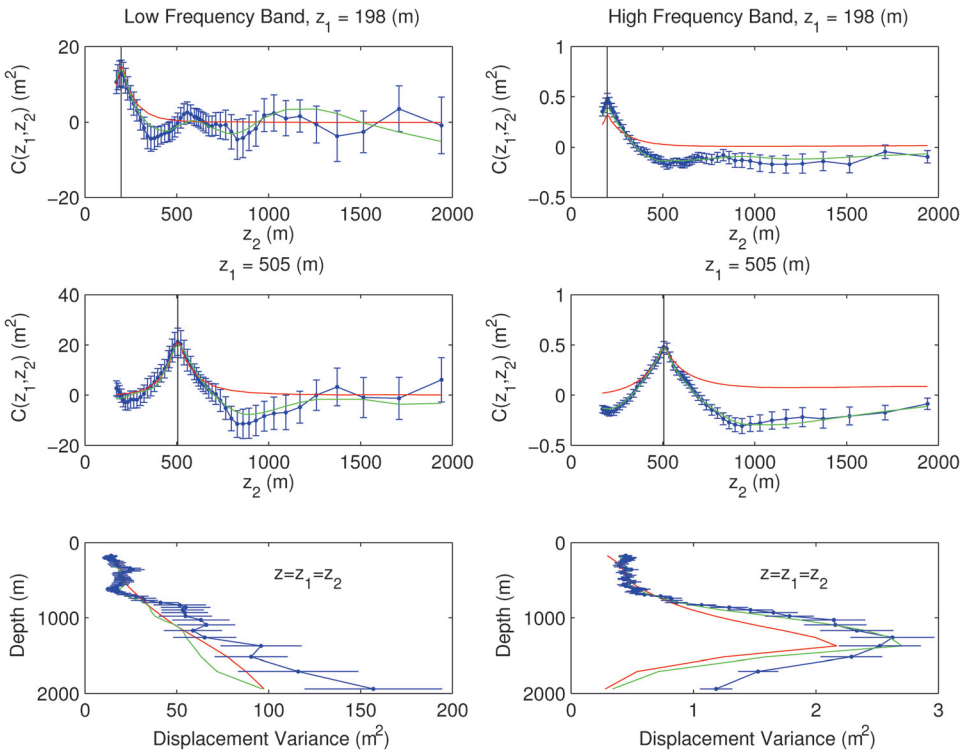


FIG. 11. Selected values of the diffuse internal wave displacement covariance function for the DVLA. The observations are plotted in blue with error bars, the fit is plotted in green, and the GM model is plotted in red. (left) The covariance for the low frequency band; (right) covariances for the high frequency band. $z_1$ is set at the values of (top) 198 and (middle) 505 m, and the covariance is plotted as a function of all the $z_2$ values. The vertical black lines indicate the $z_1$ value. (bottom) The diagonal of the covariance (i.e., the variance) is plotted as a function of depth.

distinct frequency dependence to the spectra, in which the low frequency band is somewhat different from the mid- and high-frequency bands. In particular, the peak near mode 3 is broader for the low frequency. This behavior has been noted by Fu (1981) for near inertial waves in which a GM-like spectrum fit to the observations has a mode bandwidth parameter of $j_* = 6$ compared to the standard GM value of 3.

Regarding the fits themselves, a maximum mode number of $J = 50$ was used, resulting in fits accounting for all but 17%, 2.1%, and 1.9% of the observed covariance variability in the low-, mid- and high pass-bands, respectively. Estimations using other priors gave similar fits, so the results are rather insensitive to the choices made in the estimation procedure. With regards to the maximum mode number, $J$, large values are required to fit the rapid decorrelation of the

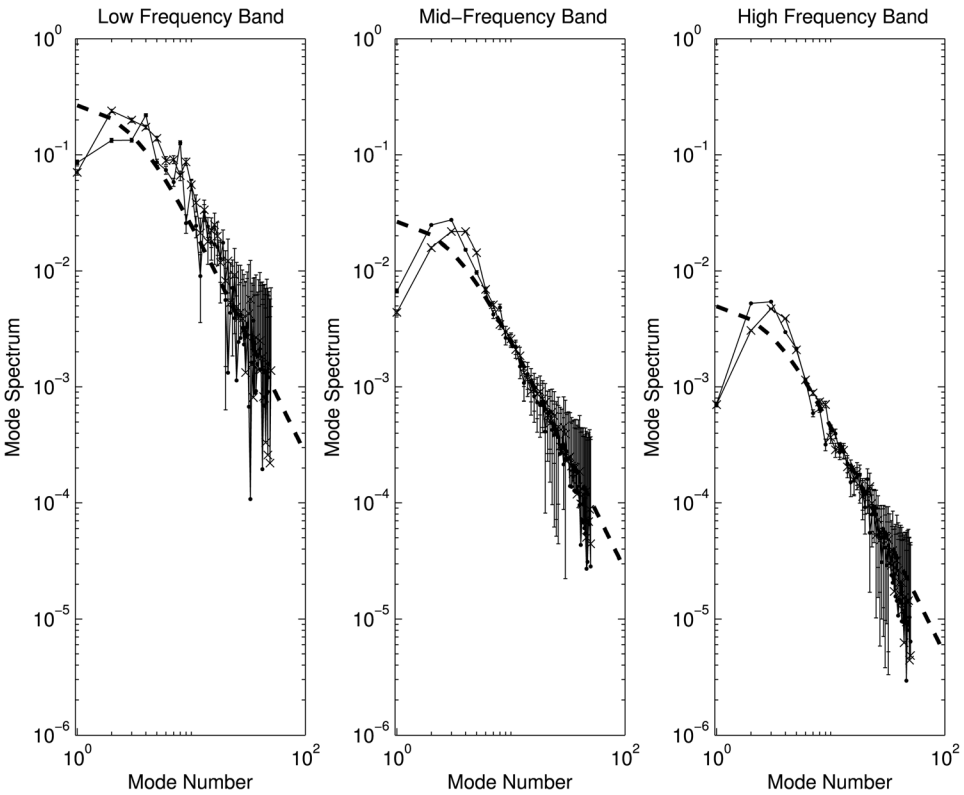


FIG. 12. Estimated displacement mode spectra for the three frequency bands at the DVLA (dots) and at T1 (crosses). For reference the GM spectrum (dash) is shown.

covariance; $J = 50$ was close to the minimum value needed to attain small residuals. The fact that the fits are not as good for the low frequencies is not surprising since the near inertial band, which dominates the low frequency variability, is quite different dynamically from the rest of the internal-wave band (Garrett, 2001). For instance, near-inertial waves are often primarily downward propagating from the surface, thereby calling into question the very idea of a mode model.

### B. Internal tides

The vertical covariance function and mode content of the diurnal and semi-diurnal internal tides are estimated here. To compute the internal tide displacement covariance functions a least square fit to the displacement time series at each depth was performed using four diurnal (O1, K1, P1, and Q1) and four semi-diurnal (M2, S2, K2, and N2) tidal frequencies, yielding separate diurnal and semidiurnal displacement time series for which the depth covariances are computed. Figure 13 shows examples of the covariance function from the DVLA, as well as an estimate of the covariance function assuming all the energy is in mode 1. Internal tide results from the T1 mooring are not similar to the DVLA, as was shown in Figs. 7 and 8, but the differences are not illuminating. The covariance in Fig. 13 shows rather large scale vertical correlations when compared to Fig. 11 for the diffuse internal waves. On the other hand the correlations are not so large as to be adequately described by mode 1 alone. If the procedure from the previous section is applied to describe the tidal covariances in Fig. 13, the fits are extremely poor and unphysical negative values for the modal spectrum are obtained. This result is due to the fact that there are strong correlations between the internal tide modes. Interestingly a shallow water internal tide analysis for the summer New Jersey continental shelf using the covariance method did yield reasonable fits (Colosi *et al.*, 2012); apparently in that case the modes were much less correlated.

Thus to better understand the modal content of the internal tide, modes are fit directly to the displacement time series (Sec. IV). Here Eqs. (1) and (4) are utilized along with the Gauss–Markov estimator, where $\mathbf{y} = \xi(z, t)$ is a vector of displacement fluctuations as a function of depth at time $t$, $\mathbf{E} = \phi_j(z)$ is a matrix of mode shapes at each depth, $\mathbf{x} = a_j(t)$ is a vector of mode amplitudes at time $t$, and $\mathbf{n}_y$ is the noise in estimating the displacement at each depth. Thus Eq. (4) is solved using the Gauss–Markov estimator at each time $t$ yielding an estimate and uncertainty for the mode amplitude $a_j(t)$. Because the internal tides are of interest, the displacement time series is bandpass filtered between $f$ and 1 cph before the estimation procedure. Regarding the priors, the matrix $\mathbf{R}$ is assumed to be diagonal with a value of 1 $m^2$ along the diagonal, and $\mathbf{S}$ is also assumed diagonal with a form that goes as one over mode number squared. Because the mode shapes, $\phi_j(z)$, for diurnal and semi-diurnal frequencies are nearly identical, this procedure is carried out for only one set of the modes yielding one time series of mode amplitudes $a_j(t)$. The mode amplitudes for the diurnal and semi-diurnal species are extracted from $a_j(t)$ by fitting the aforementioned four diurnal and semidiurnal constituents to this time series: The mean square value over time of the resulting diurnal and semi-diurnal mode amplitude time series gives the modal energy distribution shown in Fig. 14. For the calculation in Fig. 14 the maximum number of modes was taken to be $J = 50$, and as before the results were found to be insensitive to other values of this parameter as well as other choices of priors. There is a rich modal structure to the internal tide fluctuations at both diurnal and semi-diurnal frequencies, but unlike the random diffuse internal

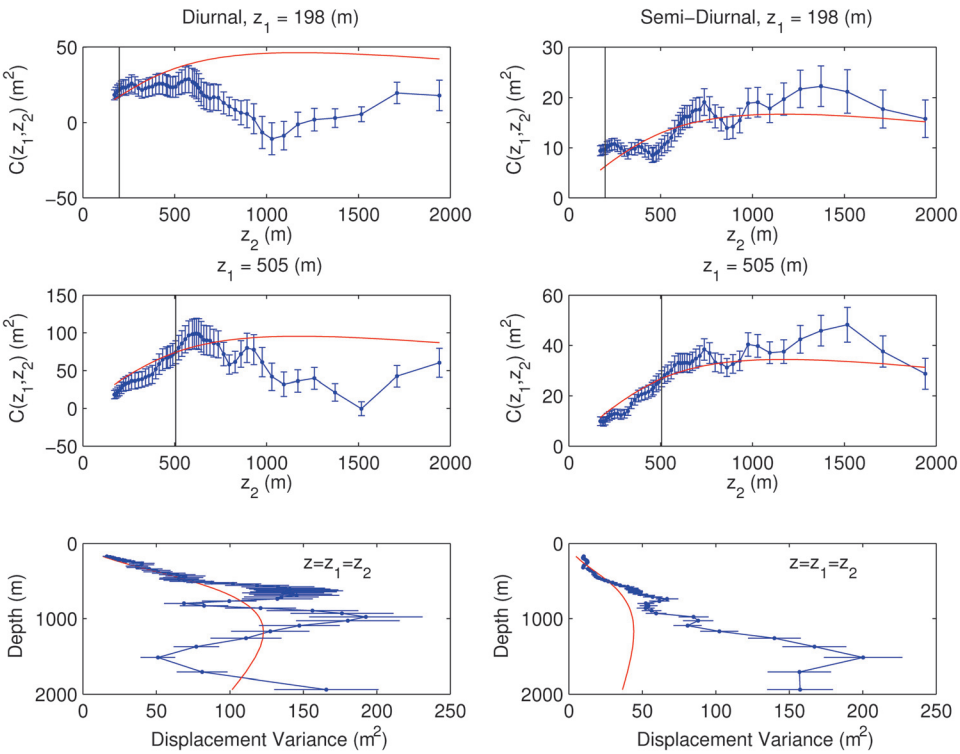


FIG. 13. Selected values of the internal tide displacement covariance function at the DVLA. The observations are plotted in blue with error bars, and a mode 1 only model is plotted in red. (left) The covariance for the diurnal tides; (right) covariances for the semi-diurnal tides. $z_1$ is set at the values of (top) 198 and (middle) 505 m, respectively, and the covariance is plotted as a function of all the $z_2$ values. The vertical black lines indicate the $z_1$ value. (bottom) The diagonal of the covariance (i.e., the variance) is plotted as a function of depth.

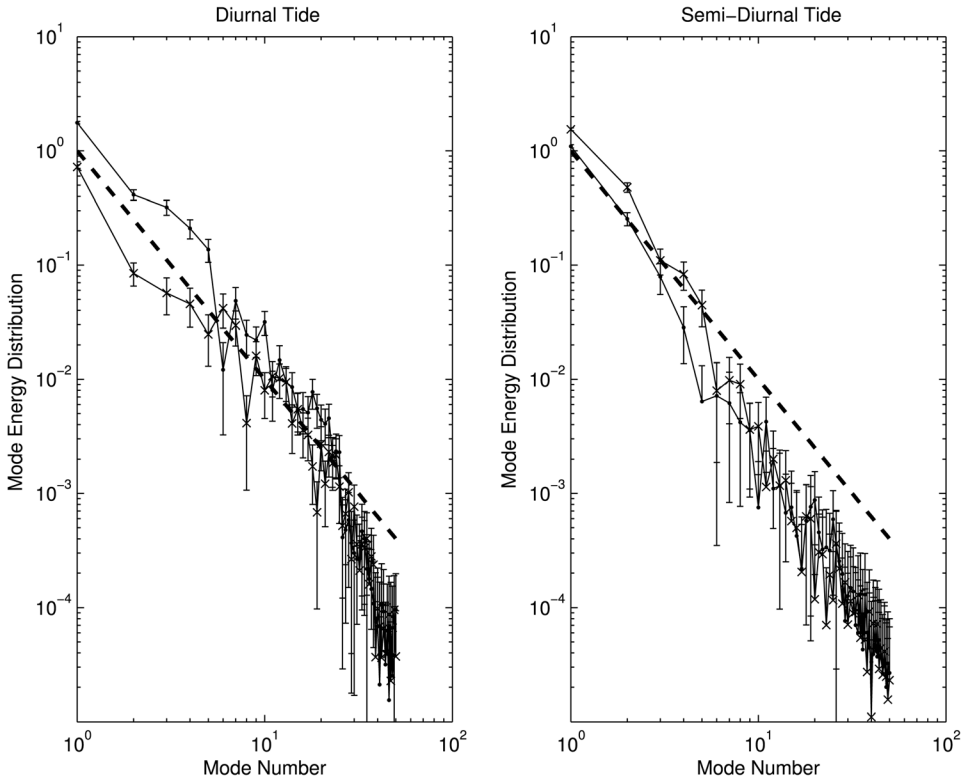


FIG. 14. Estimated displacement mode energies for the diurnal and semidiurnal internal tides at the DVLA (dots) and at T1(crosses). For reference a mode number to the minus two power scaling (dash) is shown.

waves, the internal tide modes have strong correlations. The observation of an internal tide field not dominated by mode 1 is consistent with the recent numerical modeling by Kerry *et al.* (2012) who quantified significant energy in modes 1 through 3 for Philippine Sea M2 internal tides. Note that aside from an energy level shift, in which diurnal dominates at the DVLA and vice versa for T1, the energy distributions for DVLA and T1 have very similar shapes.

### C. Spice

Last the topic of the vertical correlation scales of the PhilSea09 spicy sound-speed fluctuations is addressed. Recall that spice resolving instrumentation was only on the DVLA in the depth range 150 to 450 m (Sec. II A), so the vertical view of the spice is quite a bit smaller than that for the internal waves and tides. Figure 15 shows the normalized

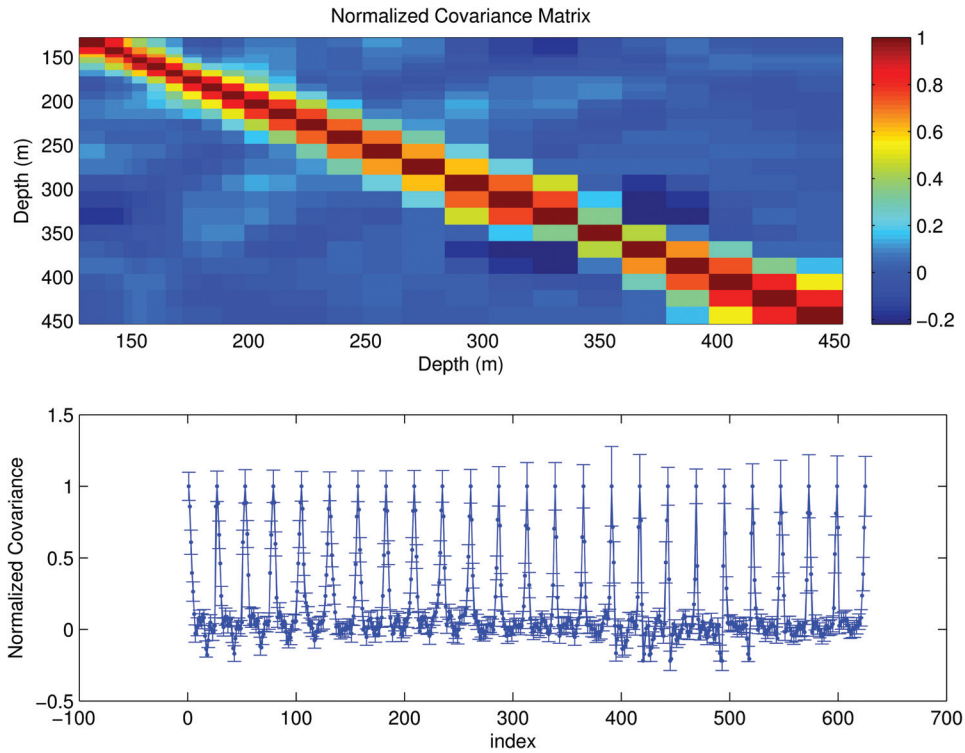


FIG. 15. Normalized depth covariance matrix of spicy sound speed fluctuations are shown in the upper panel. The lower panel shows the same matrix but the matrix has been unwrapped and error bars are shown.

covariance function for the spicy sound-speed fluctuations, $C(z_1, z_2)/[C(z_1, z_1)C(z_2, z_2)]^{1/2}$. This normalization is necessary to obtain a decent graphical view of the decorrelation properties of the spice due to the strong depth heterogeneity of the variance. Even so, it is seen that the fluctuation correlation decays extremely quickly in depth with a typical scale of tens of meters. This is in contrast to the random internal wave and internal tide fluctuations shown in Figs. 11 and 13 which have much larger scale correlations.

## V. SUMMARY AND CONCLUSIONS

The temporal and vertical scales of ocean sound-speed variability in the Philippine Sea during the spring of 2009 have been quantified in terms of important ocean processes, namely, internal waves, internal tides, and spicy thermohaline structure. This environmental information will aid in the interpretation of acoustic transmission observations that were made concurrently. To good approximation, the random internal-wave field is found to be horizontally homogeneous and isotropic and with some modification, the GM internal-wave spectrum can be used as input to acoustic fluctuation calculations. On the matter of the internal tide, it is found that they are a large source of ocean sound-speed variability, equal in strength to the random internal wave component. However, the outlook for modeling these waves is unclear. Important issues here are the internal tide nonlinearity (Fig. 6), the complex modal structure (Fig. 14), and the spatial (and perhaps temporal) inhomogeneity of the fluctuations (Fig. 7). Future work on a year-long data set from the Philippine Sea 2010–2011 will be able to properly sort out the sources of the internal tide and the processes that modulate these waves. Last on the subject of spicy thermohaline sound-speed variability, it was found that this variability was quite small except at the shallowest depths of our observations (i.e., 100–150 m). This result implies that for the PhilSea09, spice will only be important for acoustic energy which comes within 100 m of the ocean surface. Where spice did exist, the similarity between internal waves and spice frequency spectra suggests that the spice is being advected by internal-wave currents. Vertical covariance functions for the spice indicate a process with a short O(10 m) correlation length which can be compared to the internal-wave O(100 m) correlation length.

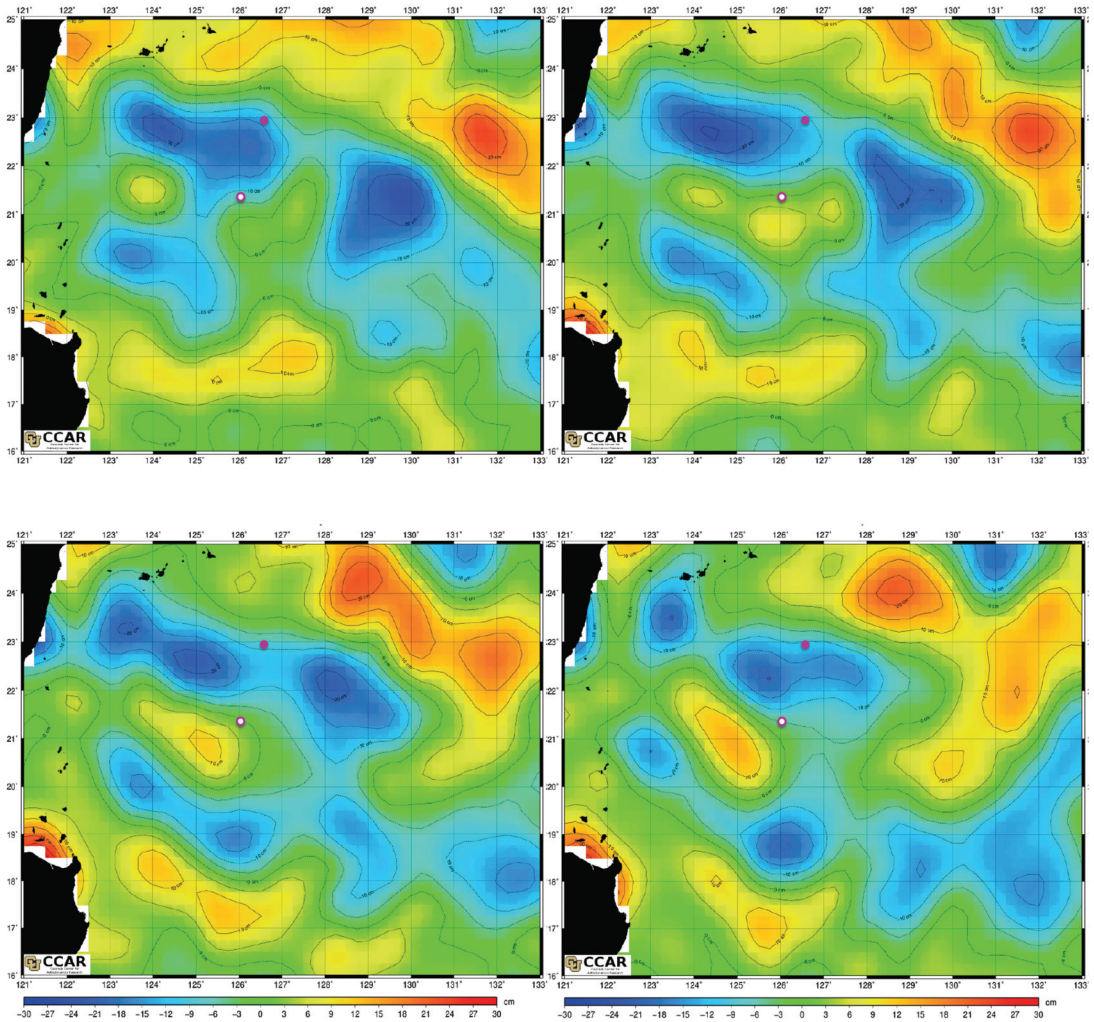


FIG. 16. Historical sea surface height fluctuation (altimetry) for the Philippine Sea during the PhilSea09 experiment. The location of the DVLA is depicted with a magenta and white dot, while the location of the T1 mooring is depicted with simply a magenta dot. The panels are for the dates (top left) 04/07/2009, (top right) 04/17/2009, (bottom left) 04/27/2009, and (bottom right) 05/07/2009. Data courtesy Colorado Center for Astrodynamics Research (CCAR; http://eddy.colorado.edu/ccar/data viewer/index).

Because of the short 33 days record, this work has focused on internal waves and spice but not eddies or sub-inertial fluctuations. These low frequency fluctuations are expected to be very strong in the Philippine Sea and they can cause significant acoustic variability. Figure 2 and calculations of sub-inertial displacement and sound speed variance (not shown) indicate that there is little evolution of the eddy field over the course of the observations. The largest, low frequency variability that is seen, is primarily in the upper 300 m of the ocean (Fig. 2). This observed surface intensification is inconsistent with a Rossby wave (Pedlosky, 1987) model of the variability (Wunsch, 1997), and thus analysis of the year long Philsea10 data will be needed to put these observations in a longer timescale context. Historical satellite altimetry (Fig. 16) shows that the PhilSea09 moorings were primarily on the edges of the eddies during the experiment, thus accounting for the small observed changes.

## ACKNOWLEDGMENTS

This work was supported by the Office of Naval Research.

[1]The low frequency correction to the GM spectrum is not based on any dynamical principle but is simply a curve fit. A dynamical interpretation of the ocean internal wave spectrum has yet to be established (Polzin and Lvov, 2011).

[2]In some cases data derived empirical modes for spice can be constructed and used to decompose the co-variance. In addition one may also decompose the observed covariance into empirical orthogonal functions (EOFs).


Beron-Vera, F. J., Brown, M. G., Colosi, J. A., Virovlyansky, A. L., Zaslavsky, G. M., Tomsovic, S., and Wolfson, M. A. (**2003**). "Ray dynamics in a long range acoustic propagation experiment," J. Acoust. Soc. Am. **114**, 1226–1242.

Colosi, J. A., Duda, T. F., Lin, T. T., Lynch, J., Newhall, A., and Cornuelle, B. C. (**2012**). "Observations of sound speed fluctuations on the New Jersey continental shelf in the summer of 2006," J. Acoust. Soc. Am. **131**(2), 1733–1748.

Cornuelle, B. D., Wunsch, C., Behringer, D., Birdsall, T. G., Brown, M. G., Heinmiller, R., Knox, R. A., Metzger, K., Munk, W. H., Spiesberger, J. L., Spindel, R. C., Webb, D. C., and Worcester, P. F. (**1985**). "Tomographic maps of the ocean mesoscale. 1 Pure acoustics," J. Phys. Oceanogr. **15**, 133–152.

Dushaw, B. D., Cornuelle, B. D., Worcester, P. F., Howe, B. M., and Luther, D. S. (**1995**). "Barotropic and baroclinic tides in the central North Pacific Ocean determined from long-range reciprocal acoustic transmission," J. Phys. Oceanogr. **25**(4), 631–647.

Dushaw, B. D., Worcester, P. F., and Dzieciuch, M. A. (**2011**). "On the predictability of mode-1 internal tides," Deep Sea Res. I **58**, 677–698.

Dzieciuch, M. A., Munk, W. H., and Rudnick, D. (**2004**). "Propagation of sound through a spicy ocean, the sofar overture," J. Acoust. Soc. Am. **116**(3), 1447–1462.

Ferarri, R., and Rudnick, D. L. (**2000**). "Thermohaline variability in the upper ocean," J. Geophys. Res. **105**, 16857–16883, doi:10.1029/2000JC900057.

Flatté, S. M., Dashen, R., Munk, W., Watson, K., and Zachariasen, F. (**1979**). *Sound Transmission Through a Fluctuating Ocean* (Cambridge University Press, Cambridge, UK), 295 pp.

Fu, L. (**1981**). "Observations and models of inertial waves in the deep ocean," Rev. Geophys. **19**(1), 141–170, doi:10.1029/RG019i001p00141.

Garrett, C. (**2001**). "What is the 'Near-Inertial' band and why is it different from the rest of the internal wave spectrum?," J. Phys. Oceanogr. **31**, 962–971.

Garrett, C., and Munk, W. (**1971**). "Internal wave spectra in the presence of fine-structure," J. Phys. Oceanogr. **1**, 196–202.

Kaneko, I., Takatsuki, Y., and Kamiya, H. (**2001**). "Circulation of intermediate and deep waters in the Philippine Sea," J. Oceanogr. **57**, 397–420.

Kerry, C. G., Powell, B. S., and Carter, G. S. (**2012**). "Effects of remote generation sites on model estimates of M2 internal tides in the Philippine Sea," J. Phys. Oceanogr. **43**, 187–204.

Levine, M. D. (**2002**). "A modification of the Garrett-Munk internal wave spectrum," J. Phys. Oceanogr. **32**, 3166–3181.

Li, Q., and Farmer, D. M. (**2011**). "The generation and evolution of nonlinear internal waves in the deep basin of the South China Sea," J. Phys. Oceanogr. **41**, 1345–1363.

Merrifield, M. A., and Holloway, P. E. (**2002**). "Model estimates of $M_2$ internal tide energetics at the Hawaiian Ridge," J. Geophys. Res. **107**, 1–12, doi:10.1029/2001JC000996.

Müller, P., and Liu, X. (**2000**). "Scattering of internal waves from finite topography in two dimensions. Part I: Theory and case studies," J. Phys. Oceanogr. **30**, 532–549.

Munk, W. (**1981**). "Internal waves and small scale processes" in *The Evolution of Physical Oceanography*, edited by B. Warren and C. Wunsch (MIT, Cambridge, MA), pp. 264–291.

Munk, W., Worcester, P., and Wunsch, C. (**1995**). *Ocean Acoustic Tomography*, Chap. 6 (Cambridge University Press).

Pedlosky, J. (**1987**). *Geophysical Fluid Dynamics* (Springer-Verlag, New York), Chap. 6.

Percival, D. B., and Walden, A. T. (**1993**). *Spectral Analysis for Physical Applications: Multitaper and Conventional Univariate Techniques* (Cambridge University Press, Cambridge, UK).

Phillips, O. M. (**1971**). "On spectra measured in an undulating layered medium," J. Phys. Oceanogr. **1**, 1–4.

Polzin, K. L., and Lvov, Y. V. (**2011**). "Towards regional characterizations of the ocean internal wave field," Rev. Geophys. **49**, 1–61, doi:10.1029/2010RG000329.

Ramp, S. R., Yang, Y. J., and Bahr, F. L. (**2010**). "Characterizing the nonlinear internal wave climate in the northeastern South China Sea," Nonlin. Processes Geophys. **17**, 481–498.

Rudnick, D. L., Jan, S., Centurioni, L., Lee, C. M., Lien, R. C., Wang, J., Lee, D. K., Tseng, R. S., Kim, Y. Y., and Chern, C. S. (**2011**). "Seasonal and Mesoscale variability of the Kuroshio near its origin," Oceanography **24**(4), 52–63.

Talley, D. L., Pickard, G. L., Emergy, W. J., and Swift, J. H. (**2011**). *Descriptive Physical Oceanography: An Introduction*, (Elsevier, Boston, MA), Chaps. 1 and 8.

Thompson, D. J. (**1982**). "Spectrum estimation and harmonic analysis," Proc. IEEE **70**, 1055–1096.

Todd, R. E., Rudnick, D. L., Mazloff, M. R., Cornuelle, B. D., and Davis, R. E. (**2012**). "Thermohaline structure in the California Current System: Observations and modeling of spice variance," J. Geophys. Res. **117**, 2156–2202, doi:10.1029/2011JC007589.

Wolfson, M. A., and Tappert, F. D. (**2000**). "Study of horizontal multipath and ray chaos due to ocean mesoscale structure," J. Acoust. Soc. Am. **107**(1), 154–162.

Worcester, P. F., Dzieciuch, M. A., Mercer, J. A., Andrew, R. K., Baggeroer, A. B., Heaney, K. D., D'Spain, G. J., Colosi, J. A., Stephen, R. A., Kemp, J. N., Howe, B. M., and VanUffelen, L. J. (**2013**). "The North Pacific Acoustic Laboratory (NPAL) deep–water acoustic propagation experiments in the Philippine Sea," J. Acoust. Soc. Am. **134**, 3359–3375.

Wunsch, C. (**1997**). "The vertical partition of oceanic horizontal kinetic energy," J. Phys. Oceanogr. **27**, 1770–1794.

Zhang, Z., Fringer, O. B., and Ramp, S. R. (**2011**). "Three-dimensional, nonhydrostatic numerical simulation of nonlinear internal wave generation and propagation in the South China Sea," J. Geophys. Res. **116**, C05022, doi:10.1029/2010JC006424.